Sheng *et al. EURASIP Journal on Advances in Signal Processing* (2016) 2016:46
DOI 10.1186/s13634-016-0345-z

EURASIP Journal on Advances in Signal Processing

RESEARCH Open Access

Feature extraction of SAR scattering centers using M-RANSAC and STFRFT-based algorithm

Hui Sheng, Yesheng Gao[†*], Bingqi Zhu, Kaizhi Wang and Xingzhao Liu[†]

Abstract

This paper introduces a modified random sample consensus (M-RANSAC) and short-time fractional Fourier transform (STFRFT)-based algorithm for feature extraction of synthetic aperture radar (SAR) scattering centers. In this algorithm, the range migration curve (RMC) of a scattering center is formulated as a parametric model. By estimating these parameters, the backscattering envelope of scattering center, corresponding to the backscattering variation in synthetic aperture time, is extracted directly from a time-domain range-compressed signal. The estimated parameters can also reconstruct the geographical location and along-track velocity of scattering centers. Thus, even without knowing explicit knowledge of platform velocity and forming a SAR image, this algorithm is capable of realizing feature extraction. To estimate parameters scatter by scatter, M-RANSAC approach is proposed as an implementary method with iterative procedure. In the iterations, fitting precision indicator (FPI) works cooperatively with construction fitness coefficient (CFC) to determine the optimal parameters of different scattering centers. Adapting this method to more general cases, STFRFT is introduced to separate the overlapped trajectories of RMCs of scattering centers. The root mean squared errors (RMSEs) of parameter estimation are close to their Cramér-Rao lower bounds (CRLB). The effectiveness of feature extraction based on the devised algorithm is validated by both simulated and real SAR data.

Keywords: SAR, M-RANSAC, STFRFT, Parameter estimation, Feature extraction

1 Introduction

Feature extraction has confirmed its usage in synthetic aperture radar (SAR) target recognition and classification, where a given target is classified as a specific target type by feature matching over the known database [1–5]. In fact, the high-frequency scattering response of a target is well approximated as a sum of response from individual scattering centers [6]. The attributes of these scattering centers, including scattering mechanism, location, and velocity, are physically relevant to those of the target [7]. Thus, to characterize target properties, feature extraction of corresponding scattering centers is a meaningful approach.

Interested attributes for each scattering center generally include backscattering envelope, geographical location, and the relative velocity between radar platform and scattering center. Backscattering envelope indicates the backscattering variation of a scattering center within synthetic aperture time. Illuminated by radar signals, some targets, like metallic surfaces, have a very directive backscattering pattern or can be sensitive only to a singular frequency (anisotropic scatters or dihedral corner reflectors). Oppositely, some targets like trihedral corner reflectors have isotropic patterns. It leads to a stable backscattering during the acquisition. Therefore, the backscattering envelope can be the feature of major concern to characterize target properties, especially when a wide-angle SAR is operated [8]. Moreover, the geographical location and relative velocity are equivalently important, since the location denotes the cross-track and along-track positions while the relative velocity reflects the along-track speed.

To extract the attributes of scattering centers, a family of time-frequency analysis (TFA) approaches has been devised. They use Wigner-Ville decomposition [9],

*Correspondence: ysgao@sjtu.edu.cn
[†]Contributed equally
School of Electronic Information and Electrical Engineering, Shanghai Jiao Tong University, 800 Dongchuan Road, 200240 Shanghai, China

wavelet transforms [10], and Fourier transform [8, 11] to realize feature extraction. Starting with spectrum of SAR imagery, these methods are constrained with knowing explicit knowledge of platform velocity and forming a SAR image first. Free from SAR image formation, another group of approaches can directly extract the feature from the spectrum of raw data. These methods rely on spectral estimation and include parametric [12–14], nonparametric [15–17], and semi-parametric approaches [18]. However, sometimes, the spectrum may wrap around azimuth frequency as a result of ambiguity [19]. Since the aforementioned methods start with the spectrum, it may degrade the effectiveness of feature extraction.

In this paper, we propose an innovative algorithm to realizes feature extraction. Starting with a time-domain range-compressed signal, this algorithm establishes its main contribution as the signal-level ambiguity-free feature extraction of scattering centers. The realization of feature extraction without knowing explicit knowledge of platform velocity and forming a SAR image provides additional novelty of this algorithm. The procedure of this algorithm is detailed as follows. First, a parametric model is presented to describe the range migration curve (RMC) of scattering center in a range-compressed signal of SAR raw data. Then, using the points extracted from the contour of the range-compressed signal, an modified random sample consensus (M-RANSAC)-based algorithm is developed to estimate the parameters scatter by scatter. Within the method, fitting precision indicator (FPI) works cooperatively with construction fitness coefficient (CFC) to determine the optimal parameters of different scattering centers through iterations. Given the estimated parameters, the backscattering envelopes can be extracted from the range-compressed signal. Along with the backscattering envelopes, geographical location and relative velocity can also be reconstructed. However, the performance of M-RANSAC-based algorithm may be degraded when the trajectories of RMCs are overlapped in the range-compressed signal. To guarantee the effectiveness in more general cases, a trajectories separation method based on STFRFT [20] is proposed, further improving the M-RANSAC-based algorithm in feature extraction.

This paper is organized as follows. Section 2 reviews the mathematical expression of received signal and models the RMC of scattering center. Section 3 describes the M-RANSAC-based algorithm for feature extraction of SAR scattering centers. Section 4 introduces a STFRFT-based trajectories separation method. An enhanced M-RANSAC algorithm embedded with this STFRFT-based method is also detailed in this section. Section 5 discusses the root mean squared error and Cramér-Rao bounds of the parameter estimation. Section 6 presents the experimental results to validate the performance of the algorithm in feature extraction and demonstrates the usage of extracted feature in target recognition and classification. In the end, Section 7 concludes this paper.

2 Mathematical model

The demodulated received signal is the superposition of those of multiple scattering centers, the expression can be written as:

$$s(\tau,\eta)=\sum_{i=1}^{M}\sigma_i(\eta-\zeta_i)\,w_r\left(\tau-\frac{2R_i(\eta)}{c}\right)w_a(\eta-\zeta_i)\times\exp\left\{-j\frac{4\pi R_i(\eta)}{\lambda}\right\}\exp\left\{j\pi k_r\left(\tau-\frac{2R_i(\eta)}{c}\right)^2\right\} \tag{1}$$

in which M is the number of overall scattering centers in the illuminated scene, τ and η represent the fast time and slow time, respectively, c is the speed of light, k_r stands for frequency modulation (FM) rate of the transmitted chirp signal, and λ is the carrier wavelength. w_r denotes the range envelope which is usually considered as a rectangle function for chirp signal, and w_a means the azimuth beam pattern which is normally a sin-squared function. ζ_i, R_i, and σ_i are defined as the ith scattering center's beam center time, the instantaneous slant range, and the complex backscattering envelope, respectively. After matched filtering in range direction, the range-compressed signal of (1) can be expressed as:

$$s_{rc}(\tau,\eta)=\sum_{i=1}^{M}\sigma_i(\eta-\zeta_i)p_r\left\{\tau-\frac{2R_i(\eta)}{c}\right\}w_a(\eta-\zeta_i)\times\exp\left\{-j\frac{4\pi R_i(\eta)}{\lambda}\right\}. \tag{2}$$

Here, $p_r\left\{\tau-\frac{2R_i(\eta)}{c}\right\}$ is a sinc function. For a single pulse, the peak locates at $\frac{2R_i(\eta)}{\mathrm{c}}$. The locations of these peaks decide the trajectory of the RMC during synthetic aperture time. To implement RMC fitting, $R_i(\eta)$ which indicates the instantaneous slant range between antenna phase center (APC) and the scattering center should be well understood. As show in Fig. 1, $R_i(\eta)$ can be formulated as:

$$R_i(\eta)=\sqrt{R_{0i}^2+V_{ri}^2(\eta-\eta_{0i})^2}, \tag{3}$$

where the ith scattering center has the nearest slant range R_{0i} at the time η_{0i} and relative velocity V_{ri} between APC and itself. Consider some scattering centers may be moving target, $V_{ri}=V-v_{ai}$ may not be the same as platform speed V (see Fig. 1). To simplify the further derivation, $R_i(\eta)$ is approximated with Taylor's series. In squint mode, $R_i(\eta)$ should be expanded at ζ_i rather than η_{oi}. Let $\eta_{ci}=$

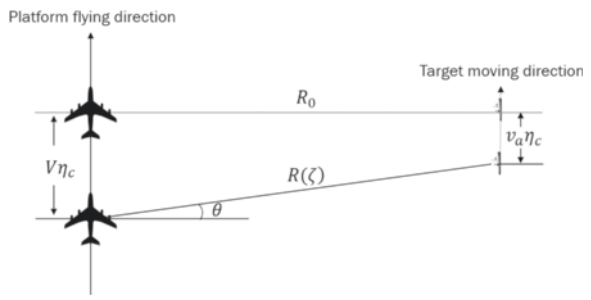

Fig. 1 SAR raw data acquisition geometry on slant range plane

$R_{0i}\tan\theta/V_{ri}$ be the offset between zero doppler time η_{oi} and beam center time ζ_i, which yields:

$$\zeta_i = \eta_{0i} - \eta_{ci}. \tag{4}$$

(3) is expanded by Taylor's series at ζ_i:

$$R_i(\eta) = R(\zeta_i) - V_{ri}\sin\theta(\eta-\zeta_i) + \frac{V_{ri}^2\cos^2\theta}{2R(\zeta_i)}(\eta-\zeta_i)^2. \tag{5}$$

Since we assume both the exposure time and the squint angle are moderate, the terms up to quadratic order in (5) are sufficient to model a RMC precisely.

Define a new coordinate:

$$\vec{\psi} = (X,Y)^T = \left(\frac{2\gamma R_i(\eta_n)}{c}, \eta_n\right), \tag{6}$$

in which the subscript n represents discrete sampling and γ scales fast time $2R_i(\eta_n)/c$ to a similar scale of magnitude of slow time η_n. Here, γ=PRI $\cdot f_s$ is decided by range sampling frequency f_s and pulse repetition interval PRI. For convenience, we let $\vartheta = c/2\gamma$. Together with (5), the discrete version of the ith scattering center's RMC can be modeled as:

$$X = A_iY^2 + B_iY + C_i \tag{7}$$

where

$$\begin{aligned} A_i &= \frac{V_{ri}^2\cos^2\theta}{2\vartheta R_i(\zeta_i)} \\ B_i &= \frac{-V_{ri}R_i(\zeta_i)\sin\theta - V_{ri}^2\zeta_i\cos^2\theta}{\vartheta R_i(\zeta_i)} \\ C_i &= \frac{V_{ri}^2\zeta_i^2\cos^2\theta + 2R_i(\zeta_i)V_{ri}\zeta_i\sin\theta + 2R_i^2(\zeta_i)}{2\vartheta R_i(\zeta_i)} \end{aligned} \tag{8}$$

In this proposed algorithm, $\vec{\mu} = \{A, B, C\}$, which parameterizes the RMC of an individual scattering center, is estimated scatter by scatter. Applying the estimated $\vec{\mu}$, the backscattering envelope σ can be extracted from range-compressed signal. Along with it, the geographical information R_0 and η_0 and the relative velocity V_r will be reconstructed. The process will be detailed in the next section.

3 M-RANSAC-based feature extraction algorithm

The proposed algorithm is an iterative method to estimate $\vec{\mu}$ of different scattering centers through fitting their RMCs. Then, the estimated parameters will be used to realize feature extraction . As shown in Fig. 2, this algorithm consists of two major steps: parameter estimation and feature extraction.

In the step of parameter estimation, the observed data is extracted from the contour of the range-compressed signal. It is a mix set of "inliers" and "outliers", indicating the trajectories of RMCs. The inliers can be explained by the parameter set $\vec{\mu}$ of current scattering center, while the outliers do not fit the model and may come from other scattering centers' RMCs or noise.

To separate the inliers from the outliers and obtain the current optimal fitting RMC with parameterized representation $\vec{\mu}$, RMC construction and performance measure are implemented iteratively in this algorithm. The iterative procedure of M-RANSAC-based approach continues until the points within observed data set are classified according to their corresponding RMCs, thus scattering centers. Along with the classified points, the overall number of scattering centers M and a set of $\vec{\mu}$ corresponding to different scattering centers are obtained.

Then, the step of feature extraction starts with these classified points and the estimated $\vec{\mu}$. The location and relative velocity of scattering centers can be directly reconstructed by $\vec{\mu}$. The backscattering scattering envelopes will be extracted from the range-compressed signal. Thus, feature extraction of M scattering centers are accomplished. The details of parameter estimation and feature extraction are summarized in the following subsections.

3.1 RMC construction with hypothetical inliers

Within a single iteration, a subset of observed data is randomly selected to construct a candidate RMC with the parametric representation $\vec{\mu}_c$. However, the observed data, which is directly extracted from the contour of the range-compressed signal, is sampled by sampling frequency f_s and pulse repetition frequency 1/PRI. Thus, the original coordinate of the observed data $\vec{x} = (x,y)^T$ obviously differs from the new coordinate $\vec{\psi} = (X,Y)^T$ in (6). To locate the points of subset in the new coordinate system, a coordinate transformation should be processed first. The mapping relationship is expressed as:

$$\vec{\psi} = K\vec{x} + O, \tag{9}$$

where

$$K = \begin{bmatrix} \frac{c}{2\vartheta} & 0 \\ 0 & \text{PRI} \end{bmatrix} \text{ and } O = \begin{bmatrix} \frac{R_s}{\vartheta} \\ \eta_s \end{bmatrix}. \tag{10}$$

Here, η_s and R_s are the minimum slow time and slant range of the given raw data, respectively.

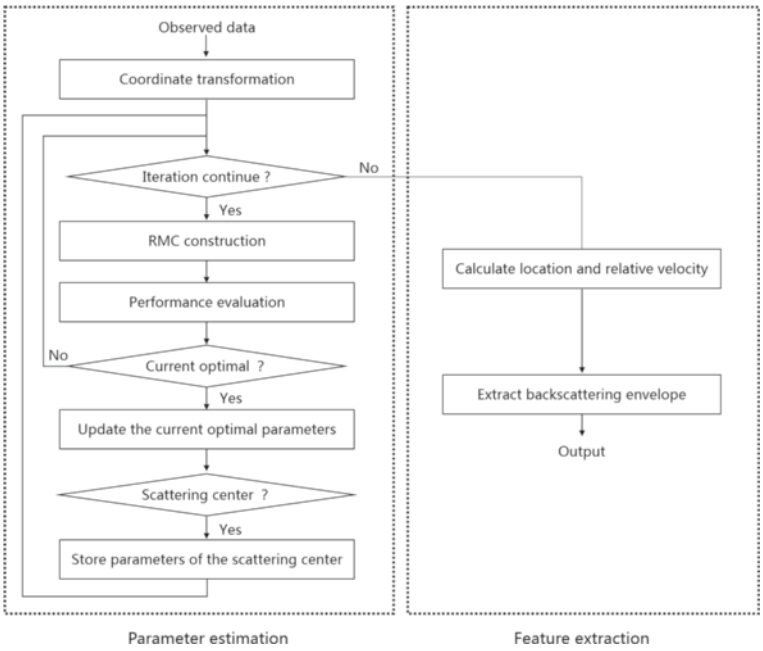

Fig. 2 Flowchart of M-RANSAC-based feature extraction algorithm

After coordinate transformation, the subset data in the new coordinate system is qualified for RMC construction. Since the degree of freedom (DOF) of (7) is three, a subset with $\vec{\psi}_1$, $\vec{\psi}_2$, and $\vec{\psi}_3$ is sufficient to calculate corresponding model parameters. $\vec{\mu}_c$ of this candidate RMC is therefore computed by:

$$\begin{aligned} A_c &= \frac{X_{12}Y_{23} - X_{23}Y_{12}}{X_{23}Y_{12}^* - Y_{12}Y_{23}^*} \\ B_c &= \frac{X_{23}Y_{12}^* - X_{12}Y_{23}^*}{Y_{23}Y_{12}^* - Y_{12}Y_{23}^*} \\ C_c &= X_1 - A_cY_1^2 - B_cY_1 \end{aligned} \tag{11}$$

in which

$$X_{ij} = X_i - X_j \text{ and } X_{ij}^* = X_i^2 - X_j^2 \tag{12}$$

The accurate construction mainly depends on the accuracy of the selected points to solve (11). Only when $\vec{\psi}_1$, $\vec{\psi}_2$, and $\vec{\psi}_3$ come from the same RMC, this constructed $\vec{\mu}_c$ can be the parametric representation of a scattering center. However, the randomly chosen points might belong to different RMCs or be just noise points. Therefore, to assess the performance of this constructed RMC, a measure needs to be established in the iterations.

3.2 Performance measure establishment based on quadratic orthogonal distance

In this subsection, a double-measure system is developed to evaluate the performance of a candidate RMC. To deal with the situation that selected points come from different RMCs or are noise points, CFC, which denotes the number of points in observed data set can be explained by the candidate RMC with $\vec{\mu}_c$, is introduced. Another measure, called FPI, is proposed to assure that a more precise RMC will be chosen when two candidate RMCs share the same CFC.

To judge whether a point can be explained by the candidate RMC, quadratic orthogonal distance (QOD) between a point and a curve is developed. The qualification of a point is decided by its QOD to the RMC with a specific threshold value. Other than the least-squares distance, QOD is defined as the minimum connecting length from a point to the given curve, which is more precise in practical applications [21]. To obtain this distance, the geometric feature of RMC is further analyzed. After coordinate transformation, RMC can be considered as a parabola with the vertex at $\vec{\psi}_{ct} = \left(C - \frac{B^2}{4A}, -\frac{B}{2A}\right)$. According to (7), the mathematical expression of RMC can be written as:

$$X - \left(C - \frac{B^2}{4A}\right) = A\left(Y + \frac{B}{2A}\right)^2. \tag{13}$$

As shown in Fig. 3, $\vec{\psi}_g$ is a point in the observed data. To calculate the QOD between $\vec{\psi}_g$ and a candidate RMC parameterized with $\vec{\mu}_c$, $\vec{\psi}_p$, which is the closest projection of $\vec{\psi}_g$ on the RMC, should be located. Define $\vec{\psi}_g = (X_g, Y_g)$ and $\vec{\psi}_p = (X_p, Y_p)$. Since $\vec{\psi}_p$ locates on the RMC, an equation can be obtained:

$$f_1(X_p, Y_p) = A_cY_p^2 + B_cY_p + C_c - X_p = 0 \tag{14}$$

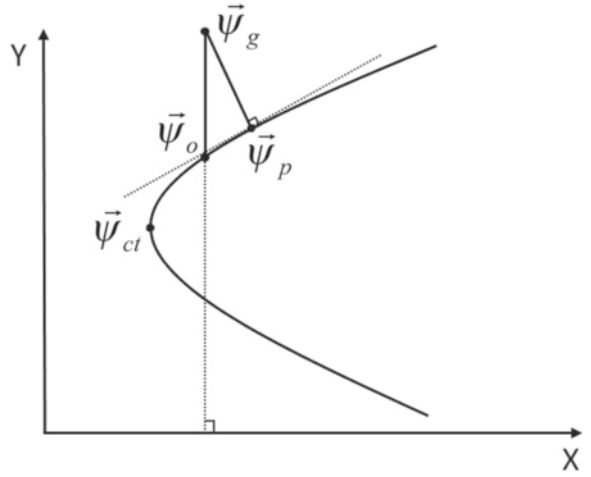

Fig. 3 Quadratic orthogonal distance to a curve

Moreover, the connecting line of $\vec{\psi}_g$ and $\vec{\psi}_p$ is perpendicular to the tangent line of the RMC at the point $\vec{\psi}_p$. This relationship can be formulated as:

$$\frac{dY}{dX}\cdot\frac{Y_g-Y_p}{X_g-X_p}=\frac{1}{2A_cY_p+B_c}\cdot\frac{Y_g-Y_p}{X_g-X_p}=-1. \quad (15)$$

Rewriting the above equation, it yields:

$$f_2\left(X_p,Y_p\right)=\left(Y_g-Y_p\right)+\left(X_g-X_p\right)\left(2A_cY_p+B_c\right)=0. \quad (16)$$

Combining (14) and (16) into a quartic equation will result in maximum four solutions. Generally, the solution with the minimum geometric distance to $\vec{\psi}_g$ is chosen as the optimal projection $\vec{\psi}_p$. However, this numerical method is not stable. To optimize the calculation, Ahn [21] proposes a generalized Newton-Raphson method to locate the closest projection point. It is an efficient iterative method which converges quickly. Given the functions $f_1\left(X_p,Y_p\right)$ and $f_2\left(X_p,Y_p\right)$, we define the derivative matrix $\boldsymbol{D}$, the current approximate result $\vec{\psi}_k$, and a more accurate approximation $\vec{\psi}_{k+1}$ to compute $\vec{\psi}_p$. The process of iterations can be presented as:

$$\begin{aligned}\boldsymbol{D}\Delta\vec{\psi}&=-f\left(\vec{\psi}_k\right)\\ \vec{\psi}_{k+1}&=\vec{\psi}_k+\Delta\vec{\psi}\end{aligned} \quad (17)$$

where

$$\boldsymbol{D}=\begin{pmatrix}\frac{\partial f_1}{\partial X_p} & \frac{\partial f_1}{\partial Y_p}\\ \frac{\partial f_2}{\partial X_p} & \frac{\partial f_2}{\partial Y_p}\end{pmatrix}=\begin{pmatrix}-1 & 2A_cY_p+B_c\\ -2A_cY_p-B_c & -1+2A_c\left(X_g-X_p\right)\end{pmatrix} \quad (18)$$

An initial value $\vec{\psi}_0$ is given in Fig. 3, and its expression is:

$$\vec{\psi}_0=\begin{cases}\begin{pmatrix}C_c-\frac{B_c^2}{4A_c}\\ -\frac{B_c}{2A_c}\end{pmatrix} & if\ X_g\le C_c-\frac{B_c^2}{4A_c}\\ \begin{pmatrix}X_g\\ \operatorname{sign}\left(Y_g+\frac{B_c}{2A_c}\right)\sqrt{\frac{X_g+\frac{B_c^2}{4A_c}-C_c}{A_c}}-\frac{B_c}{2A_c}\end{pmatrix} & if X_g>C_c-\frac{B_c^2}{4A_c}\end{cases} \quad (19)$$

Equation 17 starts its iteration with the initial value $\vec{\psi}_0$ and ends when $|\Delta\vec{\psi}|$ is no more than a given threshold. During the iterations, parameters related to $\vec{\psi}_p$ in (18) are assigned with the value of the current iterative result $\vec{\psi}_k$, and the final closest projection $\vec{\psi}_p$ is set to be $\vec{\psi}_k$ when the iterations end. Therefore, we define the square Euclidean distance between $\vec{\psi}_p$ and $\vec{\psi}_g$ as the QOD of $\vec{\psi}_g$:

$$\text{rho}=|\vec{\psi}_g-\vec{\psi}_p|^2. \quad (20)$$

When rho of $\vec{\psi}_g$ stays no more than the given threshold rho_thr, this point is regarded as an inlier, otherwise an outlier. The overall number of inliers $N\left(\vec{\mu}_c\right)$ within the observed data is denominated as CFC. As shown in Fig. 4, this measure utilizes the number of inliers to define the fitting degree of the candidate RMC. To evaluate the degree of matching between the inliers and the candidate RMC, FPI is introduced as:

$$\chi(\mu)=-\sum_{k=1}^{N}\varepsilon\left(\text{rho\_thr}-\text{rho}_k\right)\cdot\text{rho}_k. \quad (21)$$

in which ε means unit step function. FPI, which is the negative overall QOD of inliers, is known as the accuracy of fitting. It works cooperatively with CFC to locate the optimal candidate RMC with the largest number of inliers and best fitting precision. Conventional RANSAC-based algorithm [22] only considers CFC as measure without applying weighting for inliers' QOD and the maximum likelihood estimation sample consensus (MLESAC)-based method [23] obtains the overall error with a computationally complicated process. They fail in either accuracy or efficiency. The double-measure system of CFC and FPI in this algorithm steps out of this dilemma and achieves a balance between precision and efficiency.

As shown in Fig. 5, the comparative tests are conducted to evaluate this double-measure system. In the test, each set of observed data contains 100 inliers and 200 outliers (see Fig. 5a). Those inliers can be explained by a RMC with the parameter set $\vec{\mu}=\{0.2,0,4\}$, while the outliers do not fit the RMC and surpass the QOD threshold rho_thr $=0.5$ to this RMC. There exists 100 sets of observed data in all. Among them, the inliers are fixed while the outliers are randomly generated which may

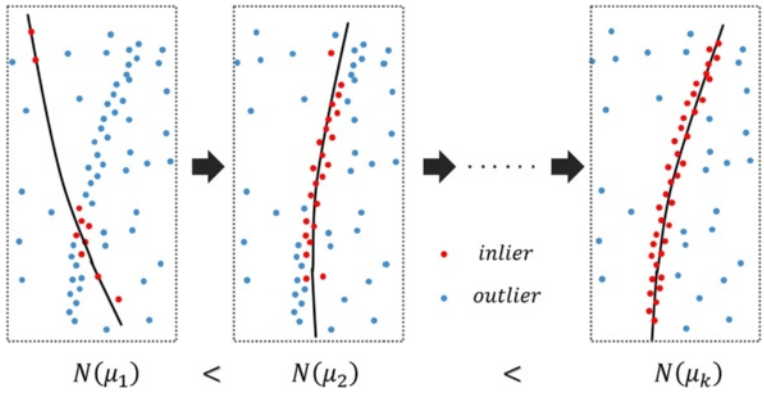

Fig. 4 Construction fitness coefficient (the number of inliers for given μ_k)

change from set to set. Based on the observed sets, 100 Monte-Carlo tests are conducted with iterative times 50, 100, 150 and 200. First, the average Euclidean norm of parameter set $\vec{\mu}$'s estimation error $\|\Delta\hat{\mu}\|$ versus iterative times are provided when the RMC is fitted by three different algorithms respectively. As shown in Fig. 5b, both the estimation accuracy and the convergence rate of MLESAC and M-RANSAC methods outperform those processed by RANSAC method. And, the estimation accuracy of the M-RANSAC method is surpassed by that of the MLESAC method. However, the superiority of MLESAC's performance costs heavy computational burden. In this paper, the computational times on a desktop PC (i5-3210M CPU at 2.5 GHz and DDR3 RAM at 8 GB) corresponding to iterative times are listed in Fig. 5c. According to this figure, we can tell the computational efficiency of MLESAC is obviously surpassed by those of the M-RANSAC and RANSAC methods. Therefore, to balance the accuracy and efficiency, the application of M-RANSAC algorithm may be the optimal choice for RMC fitting, and the

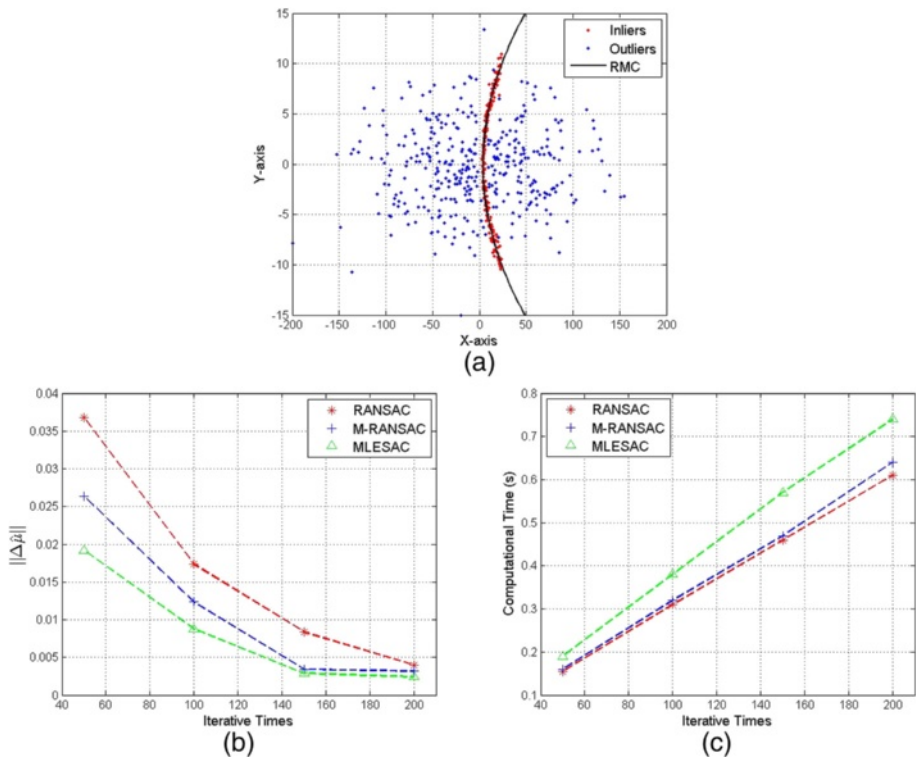

Fig. 5 Performance evaluation of the double-measure system in M-RANSAC algorithm. **a** The set of observed data. **b** Estimation accuracy compared with other measures. **c** Computational time compared with other measures

superior performance of this double-measure system is validated.

In the next subsection, M-RANSAC approach will integrate the measures and RMC construction into the iterative process of parameter estimation.

3.3 Iterative procedure of parameter estimation in M-RANSAC-based approach

The iterative process of proposed algorithm starts with a set of observed data *D_set*. It contains the points extracted from the contour of range compressed results and indicates the RMC trajectories of different scattering centers. This set also inevitably contains many noise points introduced by undesired background information. M-RANSAC-based algorithm is proposed to classify the groups of points corresponding to different scattering centers, get rid of existing noise, and realize parameter estimation of these RMCs simultaneously. The pseudocode of this process is displayed in Fig. 6. It consists of iterations of two levels: point-level iterations and scatter-level iterations. In the point-level iterations, a parametric RMC with optimal CFC and FPI is located to explain a scattering center. Then, the scatter-level iterations will lock all these RMCs in a range-compressed signal scatter by scatter.

```
Given:
  D_set     – the set of observed data
  min, max – the minimum and maximum iteration times
  m         – maximum non-updating times
  rho_thr   – the threshold QOD to define an inlier
  N_thr     – the minimum number of inliers to confirm a RMC
  CONT      – iteration proceeding factor
Output:
  M  – the number of scattering center
  set  – groups of classified points according to scattering centers they belong to
  setμ – the set containing the parametrized representation of fitted RMCs
while CONT==1 {
  Let M, iteration, and bestN = 0
  Let non_upd = infinity
  while iteration ≤ min  ||  (iteration ≤ max && non_upd ≤ m ){
    iteration+1, non_upd+1
    μ_c = RMC construction with 3 randomly selected points from D_set
    Calculate rho for every point in D_set to obtain an inlier data set set(μ_c)
        N(μ_c) = construction fitness coefficient with μ_c
        χ(μ_c)  = fitting rank indicator with μ_c
    if (N(μ_c) ≥ N_thr && N(μ_c) > BestN ) || (N(μ_c) == BestN && χ(μ_c) > best χ){
      Define a current optimal fitting RMC, and update judgment conditions:
        non_upd = 0
        Bestμ   = μ_c
        BestN   = N(μ_c)
        Bestχ   = χ(μ_c)
        Bestset = set(μ_c)
        recalculate m
      }
    }
  CONT = 0
  if BestN  ≥ N_thr {
   Confirm a new scattering center and store the relevant information:
     M+1
     setμ(M)  = Bestμ
     set(M)   = Bestset
   Iteration should continue to find another scattering center:
     CONT = 1
     clear Bestset from D_set
  }
 }
return M, setμ and set
```

Fig. 6 The pseudocode of parameter estimation in M-RANSAC-based approach

To begin with, the minimum iterative times min, maximum iterative times max, the threshold QOD to define an inlier rho_thr and the threshold number of inliers to confirm a scattering center N_thr should be preestablished. What is more, we should initialize maximum non-updating times m to infinite, the number of scattering center M to zero, and the iteration proceeding factor CONT to 1.

A point-level iteration starts with randomly selecting three points from *D_set* to construct a candidate RMC. The $\vec{\mu}_c$ of this RMC is computed with (9) and (11). Then, according to subsection 3.2, the QOD between every point in the *D_set* and this candidate RMC are calculated and denoted by rho. The points whose rho stay no more than rho_thr are defined as inliers and stored in set($\vec{\mu}_c$). Then, CFC $N(\vec{\mu}_c)$ and FPI $\chi(\vec{\mu}_c)$ of this candidate RMC can be computed by (20) and (21).

This RMC can be regarded as the current optimal one in two cases. The CFC $N(\vec{\mu}_c)$ exceeds that of the former optimal *BestN*, or the FPI $\chi(\vec{\mu}_c)$ goes over that of former optimal $Best\chi$ under the circumstance that $N(\vec{\mu}_c)$ equals *BestN*. When the conditions are satisfied and the current optimal is renewed, not only $Best\mu$, *BestN*, $Best\chi$, and *Bestset* are updated in line with the values of current optimal RMC but also the maximum non-updating times m will be recalculated. The point-level iteration stops when iterative times *iteration* exceed max or non-updating times *non_upd* surpass m. An additional minimum iteration times min is used to remain the stability.

In scatter-level iterations, a new scattering center will be confirmed when the output of the point-level iterations *BestN* goes beyond N_thr. At this time, the number of recovered scattering centers M is updated. $Best\mu$ and *Bestset* are stored in $set\mu(M)$ and $set(M)$. The idea of CLEAN technique [24, 25] are taken, and the points in *Bestset* will be subtracted from *D_set*. Another point-level iterations will be processed to locate the next RMC. Oppositely, if the point-level iteration fails to locate a scattering center, the remaining points in observed data set are considered as noise points. Thus, the scatter-level iterations stop by setting CONT $= 0$.

After the two-level iterations, the total number of scattering centers M is determined, the points of inliers are classified in *set*, and the parametric representation μ of scattering centers are estimated and saved in $set\mu$. These data will help to realize feature extraction for dominant scattering centers of the targets in the next subsection.

3.4 Feature extraction based on estimated parameters

To realize feature extraction, a vector $\vec{T}_i$ is established to cover the interested information of the ith scattering center, $\vec{T}_i = \{ R_{0i},\ \eta_{0i},\ V_{ri},\ \sigma_i(\eta - \xi_i) \}$. In this vector set, R_{0i} and η_{0i} present the geographical location in both cross-track direction and along-track direction. V_{ri}, which is the

relative velocity between the radar platform and scattering center, indicates the possible along-track speed of the scatter. They can be reconstructed using the estimated $\vec{\mu}_i$ in $set\mu(i)$:

$$\begin{aligned} R_{oi} &= \frac{\vartheta\left(4A_iC_i - B_i^2\right)\cos\theta}{2A_i\left(2-\tan^2\theta\right)} \\ \eta_{0i} &= -\frac{B_i}{2A_i} + \frac{\sin 2\theta - 2\tan\theta}{4A_i}\sqrt{\frac{4A_iC_i - B_i^2}{2-\tan^2\theta}} \\ V_{ri} &= \vartheta\sqrt{\frac{4A_iC_i - B_i^2}{2\cos^2\theta - \sin^2\theta}}. \end{aligned} \tag{22}$$

In broadside case, $\sin\theta$ and $\tan\theta$ equal zero. (22) degrades to a simpler formula:

$$\begin{aligned} R_{0i} &= \vartheta\left\{C_i - \frac{B_i^2}{4A_i}\right\} \\ \eta_{0i} &= -\frac{B_i}{2A_i} \\ V_{ri} &= \vartheta\sqrt{2A_iC_i - \frac{B_i^2}{2}}. \end{aligned} \tag{23}$$

Knowing R_{0i}, η_{0i}, and V_{ri}, compressed range envelope p_r, azimuth beam pattern w_a, and the phase information related to instantaneous slant range R_i are calculated. By locating inliers $set(i)$ in the range-compressed signal, the complex values along the RMC of scattering center can be extracted. According to (2), we obtain the complex backscattering envelope $\sigma_i(\eta - \zeta_i)$ by eliminating the influence of the aforementioned components in the extracted complex values. The vector set $\left\{\vec{T}_1,\ \vec{T}_2, \ldots\ \vec{T}_M\right\}$ are calculated scatter by scatter.

It is worth noting that, the process of M-RANSAC-based algorithm does not need the explicit parameters (e.g., platform velocity). However, for conventional methods of feature extraction based on SAR image formation, the platform velocity works as a crucial parameter of realizing range cell migration correction (RCMC) and azimuth matched filtering. Thus, compared with the conventional approach, M-RANSAC-based algorithm can be utilized in a more flexible way. Moreover, the proposed algorithm extracts the features directly from a range-compressed signal. Without forming SAR image, we may realize target recognition and classification directly in a signal level rather than in an image level.

When platform velocity is known and SAR image is formed, the backscattering envelope extracted by the proposed algorithm may classify targets which are similar in the gray-level SAR image. Moreover, given the platform velocity and the relative velocity between radar platform and the dominant scattering center, the along-track velocity of target can be computed. Thus, even if SAR image is formed, this feature extraction algorithm may help us to better understand the target.

4 Trajectories separation based on STFRFT

Sometimes, RMC of one scattering center may overlap that of the other. This phenomenon is called trajectories overlapping in this paper. As shown in Fig. 7a, the trajectories of T1 and T2 are mixed after range compression (to clearly state the principle, the range curve are ignored under the low-resolution assumption). In this case, M-RANSAC-based algorithm may fail in extracting interested information of T1 and T2, respectively. To solve this problem, short-time fractional Fourier transform (STFRFT) is applied to separate the overlapped trajectories. With a spatial filtering using a rectangle window, the trajectories of different scattering centers will be separated in time-fractional frequency domain. The feature extraction can be successfully proceeded afterwards.

The phase component in (2) can be written as:

$$s_\phi(\eta) = \sum_{i=1}^{M}\exp\left\{j\phi_i + j2\pi f_i\eta - j\pi K_a\eta^2\right\} \tag{24}$$

where,

$$\begin{aligned} \phi_i &= -\frac{4\pi}{\lambda}\left\{R(\zeta_i) - V_{ri}\sin\theta\zeta_i\right\} - \frac{\pi V_{ri}^2\cos^2\theta}{R(\zeta_i)}\zeta_{ri}^2 \\ f_i &= \frac{2V_{ri}\sin\theta}{\lambda} + \frac{V_{ri}^2\cos^2\theta}{R\left(\zeta_i\right)}\zeta_i \\ K_a &= \frac{V_{ri}^2\cos^2\theta}{R\left(\zeta_i\right)} \approx \frac{V_{\mathrm{ref}}^2\cos^2\theta}{R_{\mathrm{ref}}}. \end{aligned} \tag{25}$$

Here, K_a is considered as a constant. It is a reasonable assumption when the range span of processed data is moderate. f_i, related to the beam center time ζ_i, differs with the azimuth location of scattering center. Taking STFRFT of (24), it yields:

$$\begin{aligned} \mathrm{STF}_\phi(\eta,u) = \sum_{i=1}^{M}\exp\left\{j\phi_i\right\}\int_{-\infty}^{\infty}\exp\left\{j2\pi f_it - j\pi K_at^2\right\} \\ \times\, g(t-\eta)K_p(t,u)dt. \end{aligned} \tag{26}$$

where, to obtain the optimal 2D resolution [20], a Gaussian window $g(t)$ is used:

$$g(t) = \left(\pi\xi^2\right)^{-1/4}\exp\left(-\frac{t^2}{2\xi^2},\right) \tag{27}$$

in which $\xi^2 = |\sin\alpha/K_a|$, and $K_p(t,u)$ denotes the kernel function of fractional Fourier transform (FRFT) with an expression:

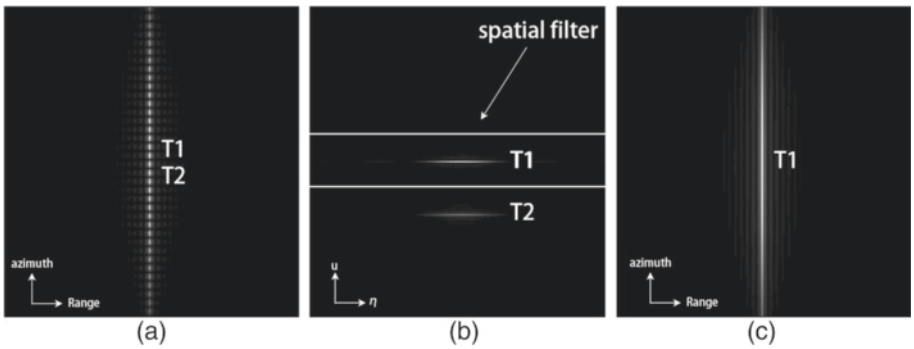

Fig. 7 Trajectories separation based on STFRFT. **a** Overlapped trajectories of T1 and T2. **b** Matched STFRFT and spatial filter of trajectories in selected range bin. **c** Separated trajectory of T1

$$K_p(t,u)=\begin{cases}\sqrt{\frac{1-j\cot\alpha}{2\pi}}\exp\left(j\frac{t^2+u^2}{2}\cot\alpha-jut\csc\alpha\right),\alpha\neq k\pi\\ \delta(u-t), \qquad \alpha=2k\pi\\ \delta(u+t), \qquad \alpha=(2k+1)\pi\end{cases} \tag{28}$$

Based on the frequency shift property of STFRFT [20], (26) becomes:

$$\begin{aligned}\mathrm{STF}_{\phi}(\eta,u)=\sum_{i=1}^{M}\exp\left\{j\phi_i+j2\pi uf_i\cos\alpha\right.\\ \left.-j2\pi f_i^2\sin\alpha\cos\alpha\right\}\mathrm{STF}_{K_a}\left(\eta,u-2\pi f_i\sin\alpha\right)\end{aligned} \tag{29}$$

where,

$$\mathrm{STF}_{K_a}(\eta,u)=\int_{-\infty}^{\infty}\exp\left\{-j\pi K_at^2\right\}g(t-\eta)K_p(t,u)dt. \tag{30}$$

Note that (30) is a matched STFRFT only when the second-order phase term is set to zero, thus, α is:

$$\alpha=\mathrm{arc\,cot}\left\{2\pi K_a\cdot N_a\mathrm{PRI}^2\right\} \tag{31}$$

where, *PRI* is the pulse repetition interval and N_a denotes the length of azimuth sample. In the real application, $N_a\mathrm{PRI}^2$ is used as the factor of coordinate transformation in digitalized computation [26, 27]. Back to (29), the STFRFT of an individual scattering center is decided by $\mathrm{STF}_{K_a}(\eta,u)$. The matched STFRFT of (30) will locate the spectrogram line of a scattering center parallel to η. For multiple scattering centers, the shift $\Delta u=-2\pi f_i\sin\alpha$ along u axis in (29) separates their energy according to their different azimuth locations. As shown in Fig. 7b, a simple spatial filter using a rectangle window will separate the energy of one scattering center from the others. After inverse STFRFT, the trajectories of scattering centers with similar range position but different azimuth location are separated (e.g., Fig. 7c).

To realize trajectories separation in feature extaction, the STFRFT-based method is embedded in the aforementioned M-RANSAC-based approach. The processing steps can be summarized as follows:

1. Select the trajectory of an isolated scattering center and estimate K_a using the points extracted from it.
2. Calculate α based on (31).
3. Execute α-angle STFRFT for a range bin.
4. Implement spatial filtering using rectangle windows.
5. Realize trajectories separation with inverse STFRFT.
6. Repeat steps 3 to 5 until the last range bin is processed.
7. For every sub-patch range compressed signal, estimate M, $set\mu$, and set using M-RANSAC approach.
8. Use the estimated M, $set\mu$, and set to compute the vector set $\left\{\vec{T}_1,\ \vec{T}_2,\ldots\ \vec{T}_M\right\}$.

5 CRLB and RMSE of parameter estimation

The parameter estimation of $\vec{\mu}$ lays the foundation for feature extraction in this algorithm. In this section, Monte-Carlo tests are conducted to obtain the root mean squared errors (RMSEs) of the estimates. To evaluate the accuracy of estimation, these RMSEs of estimators compared their theoretical minimal errors, named Cramér-Rao lower bound (CRLB). We start this section with computing the CRLBs according to observation.

The observation can be derived from (2) and (7):

$$\chi_o[n]=\Gamma\left[n;\vec{\phi}_e\right]+\omega_0[n],n=0,1,2,\ldots.N_a-1 \tag{32}$$

in which,

$$\begin{aligned}\Gamma[n;\vec{\phi}_e]=\sigma\{n\cdot\mathrm{PRI}\}w_a\{n\cdot\mathrm{PRI}\}\\ \exp\left\{-j\frac{4\pi\vartheta}{\lambda}\left(A\cdot\mathrm{PRI}^2n^2+B\cdot\mathrm{PRI}\cdot n+C\right)\right\}.\end{aligned} \tag{33}$$

Here, $\omega_0(n)$ denotes a complex white noise with zero mean and the variance of σ_0. The estimator vector $\vec{\phi}_e = [\hat{A}, \hat{B}, \hat{C}]$ contains three parameters waiting to be estimated.

According to [28], the Fisher information matrix of (32) can be calculated using the expression:

$$\left[I\left(\vec{\phi}_e\right)\right]_{ij} = \frac{1}{\sigma_o^2}\sum_{n=0}^{N_a-1}\frac{\partial\Gamma[n;\vec{\phi}_e]}{\partial\left[\vec{\phi}_e\right]_i}\frac{\partial\Gamma[n;\vec{\phi}_e]}{\partial\left[\vec{\phi}_e\right]_j} \tag{34}$$

The computation of its inverse is complicated and tedious, we omit the procedures of derivation and directly give the result:

$$\left[I(\vec{\phi}_e)\right]^{-1} = 3\left(\frac{\sigma_0\lambda}{4\pi\vartheta\Lambda}\right)^2 \begin{bmatrix} \frac{60}{\mathrm{PRI}^4\Theta_1} & \frac{60}{\mathrm{PRI}^3\Theta_2} & \frac{10}{\mathrm{PRI}^2\Theta_3} \\ \frac{60}{\mathrm{PRI}^3\Theta_2} & \frac{12\left(16N_a^2-30N_a+11\right)}{\mathrm{PRI}^2\Theta_1} & \frac{-6(2N_a-1)}{\mathrm{PRI}\Theta_3} \\ \frac{10}{\mathrm{PRI}^2\Theta_3} & \frac{-6(2N_a+1)}{\mathrm{PRI}\Theta_3} & \frac{3N_a^2-3N_a+2}{\Theta_3} \end{bmatrix} \tag{35}$$

where the Λ is the average amplitude of backscattering envelope $\sigma\{n\cdot PRI\}$ and azimuth beam pattern $w_a\{n\cdot PRI\}$. $\Theta_1 = N_a(N_a-1)(N_a-4)$, $\Theta_2 = N_a\left(-N_a^3-N_a^2+4N_a+4\right)$ and $\Theta_3 = N_a(N_a+1)(N_a+2)$. According to (35), the CRLBs of estimated parameters are the diagonal elements of inverse matrix. Thus, the CRLBs of $\hat{A}$, $\hat{B}$, and $\hat{C}$ are equal to $\left[I(\vec{\phi}_e)\right]_{11}^{-1}$, $\left[I(\vec{\phi}_e)\right]_{22}^{-1}$ and $\left[I(\vec{\phi}_e)\right]_{33}^{-1}$, respectively.

Then, 100 Monte-Carlo tests are conducted when signal-to-noise ratio (SNR) is $0, 2, 4, 6, 8$, and 10 dB, respectively. The experiments utilize the SAR simulation parameters listed in Table 1. To better exhibit the results, both RMSEs and CRLBs of the estimated parameters are expressed in decibels. As shown in Fig. 8, the RMSEs of the estimated values stay close to their CRLBs. Since CRLB is the theoretical lowest estimation error, we can conclude that the parameter estimation based on the proposed algorithm is accurate and effective. The precisely estimated parameters guarantee the subsequent process of feature extraction.

Table 1 System parameter of simulation and real data

Parameter	Simulation test	Real data experiment
Squint angle	0°	−1.584°
Signal bandwidth	150 MHz	30.111 MHz
Sample frequency	200 MHz	32.317 MHz
Pulse duration	5.12 μs	41.74 μs
PRI	1.7 ms	0.7956 ms
Platform velocity	153.3 m/s	7062 m/s
Range to scene center	7500 m	998263 m

6 Experimental results

To validate the performance of this algorithm, a series of experiments, named performance test, simulation test, and real data test, respectively, are presented in this section. In the performance test, we generate raw data of a single target when the broadside airborne SAR system operates. This raw data is added with various Gaussian white noise and then taken as the input of M-RANSAC algorithm to estimate the location and velocity of dominant scattering center. RMSE of the estimated parameters are listed corresponding to different input SNR and iterative times. Then, the scenario of multiple targets is considered in the simulation test. In the illuminated scene, three targets with different backscattering envelopes and along-track velocities are introduced. The features of dominant scattering centers are extracted from the generated data by M-RANSAC-based algorithm and compared with the theoretical ones. In addition, the potential usage of these extracted features in target recognition and classification are fully considered. In the end, the real data of RADARSAT-1 are processed to validate the performance of the proposed algorithm when the trajectories of targets are overlapped. The features of the dominant scattering centers, including locations, relative velocities, and backscattering envelopes, are extracted using both STFRFT-based trajectories separation and M-RANSAC-based feature extraction method. To verify the effectiveness of feature extraction, the reconstructed locations and velocities are compared with those obtained using conventional methods. To confirm the potential usage of these extracted features in target classification, the backscattering envelopes are used to further interpret the ships in English Bay which is located in the city of Vancouver, Canada (see Fig. 13a).

6.1 Performance test

In this subsection, raw data of a single target are simulated to evaluate the estimation accuracy. This target is a stationary one with the geographical location $R_0 = 7500$ m and $\eta_0 = 0.8717$ s. In the simulation, the system parameters are listed in the middle column of Table 1 and beam width in azimuth dimension is set to be 0.059 rad. The generated raw data are added with Gaussian white noise when the input SNR $= -10, -5, 0, 5$, and 10 dB. For each input SNR, we generate 150 sets of random Gaussian noise; thus, in total, 750 sets of observed raw data are obtained.

The M-RANSAC-based algorithm starts with those time-domain range compressed signals (see Fig. 9a). Its initial parameters are carefully designed. The scale factor

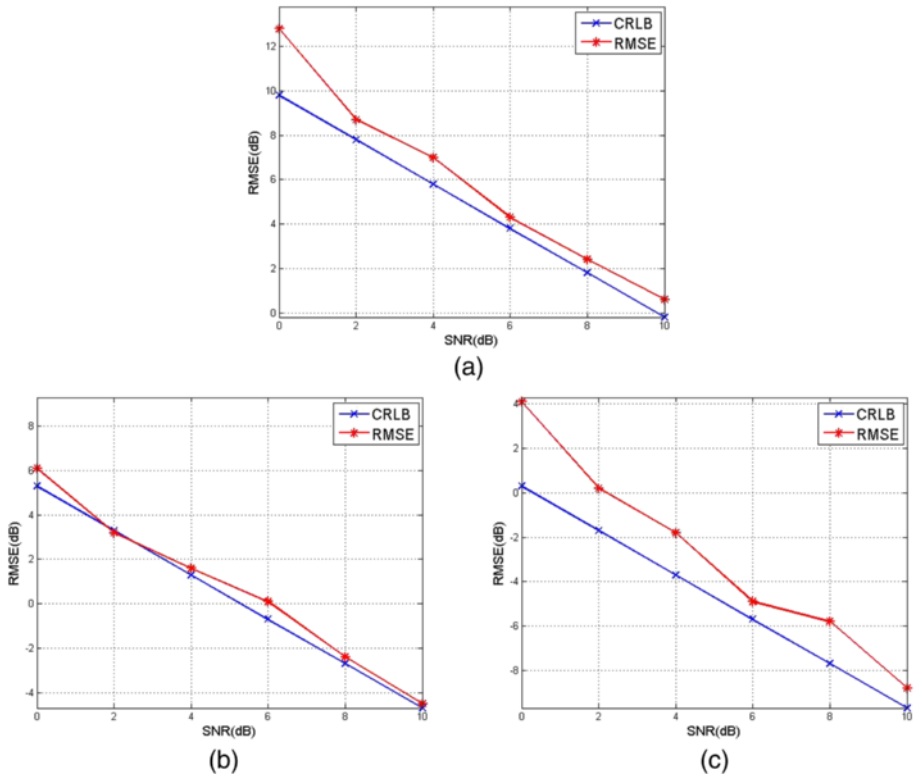

Fig. 8 RMSEs of parameter estimation and their CRLBs. **a** RMSE and CRLB of A. **b** RMSE and CRLB of B. **c** RMSE and CRLB of C

ϑ in (10) is set to be 450. The threshold of quadratic orthogonal distance rho_thr is 0.003 and the threshold number of inliers N_thr is $0.85N_a$. The overall iterative times are set to be a fixed number $T_{\text{iter}} = 50$, 100, 150, and 500. After estimating $\vec{\mu}$ for the M dominant scattering centers and classifying inliers in *set*, the geographical locations and velocity information are reconstructed based on (23). For each input SNR, 150 sets of observed raw data will output 150 sets of $\left\{\hat{R}_0,\ \hat{\eta}_0,\ \hat{V}_r\right\}$. Compared with the theoretical ones, RMSE of $\{R_0,\ \eta_0,\ V_r\}$ corresponding to different input SNR and iterative times are obtained and shown in Fig. 9b–d. According to this figure, several conclusions can be made:

(1) The estimation errors of location and relative velocity are quite limited especially when input SNR is 5 and 10 dB. Thus, We can expect a high estimation accuracy in a high-SNR case.
(2) The estimation accuracy may decrease along with the input SNR. The reasonable explanation is that a higher-level noise will impact the precision of inliers in a larger degree and thus decrease the estimation accuracy. In the performance test, this phenomenon becomes obvious when the low-SNR data is implemented.
(3) The estimation accuracy will be continuously enhanced with the increasing of iterative times until it converges. When input SNR is high, the estimation error converges fast. We can expect a high-precision output with a small number of iterative numbers. However, under low-SNR scenario, the estimation error converges slowly. max can be considerably increased to obtain relatively high-accuracy estimators. Unfortunately, there exists no SNR-related closed-form expression of max. The initial parameter max is an empirical parameter in this paper.

6.2 Simulation test

To further analyze this algorithm, the scenario of multiple targets is introduced in this subsection. According to the Li's research [12], most of man-made objects can be considered as the composition of trihedral corner reflectors and dihedral corner reflectors. Generally speaking, a trihedral corner reflector has a flat backscattering envelope during synthetic aperture time while a dihedral corner reflector has a variant one. Thus, in the simulation test, we simplify the types of targets in [8] to two: azimuth invariant target (e.g. Fig. 10a) and azimuth variant target (e.g. Fig. 10b), and their different backscattering envelopes

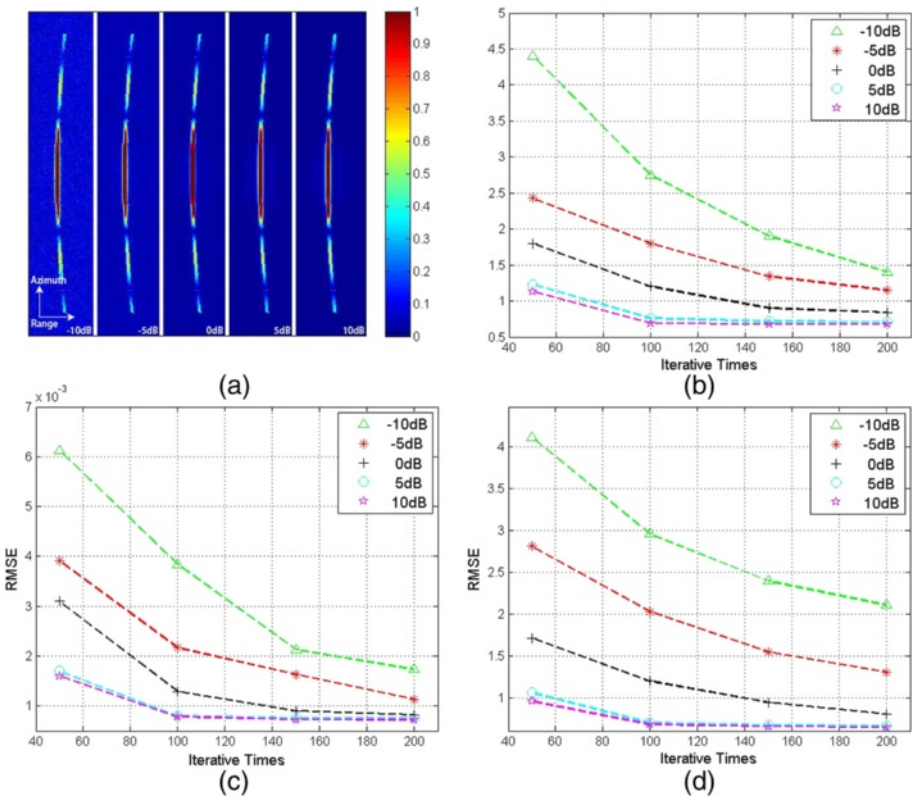

Fig. 9 Performance test. **a** Time-domain range compressed signal with different input SNR (range-compressed azimuth-time domain). **b** RMSE of R_0. **c** RMSE of η_0. **d** RMSE of V_r

are shown in Fig. 10c. In the illuminated scene, we have two azimuth invariant point targets: T1 and T2. The amplitude and phase of their theoretical backscattering envelopes are presented in Fig. 11a, b, respectively. T1 is set to be "brighter" than T2, which means it has a relatively higher backscattering coefficient or a larger radar cross section (RCS) [29]. We also have an azimuth variant point target T3, the maximum backscattering envelope of which stays lower than both T1 and T2 (see Fig. 11a). Different from T1 and T2, T3 has an inconstant phase envelope during the synthetic aperture time (see Fig. 11b). In the simulation test, these targets are customized with the size of 2 m in range by 1 m in azimuth, and their geographical locations are shown in the columns $\boldsymbol{R_0}$ and $\boldsymbol{\eta_0}$ of Table 2. Moreover, both T1 and T3 are stationary targets while T2 is a moving target with a 5.5 m/s along-track velocity. The relative speed between radar platform and targets are listed in the column $\boldsymbol{V_r}$ of Table 2.

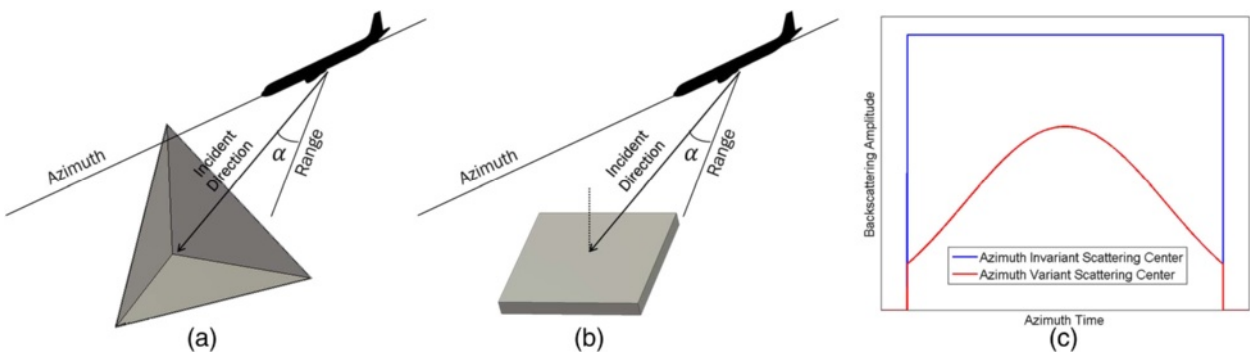

Fig. 10 Scattering centers with different backscattering envelopes. **a** Azimuth invariant scattering center. **b** Azimuth variant scattering center. **c** Backscattering envelopes of different scattering centers

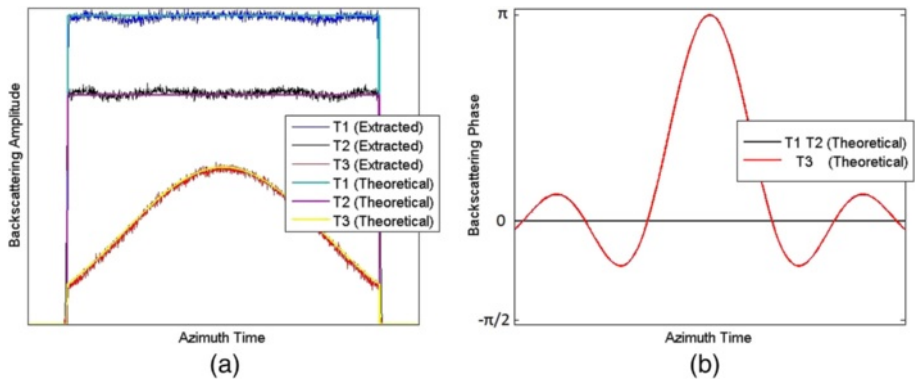

Fig. 11 Backscattering envelopes of targets. **a** Theoretical backscattering amplitude envelopes of targets and the extracted ones of dominant scattering centers. **b** Backscattering phase envelopes of targets

Using the SAR simulation parameters in Table 1, we generate the raw data of these three targets when SNR is 5 dB and beam width in azimuth dimension is 0.0785 rad. In this case, the Doppler spectrum of the range-compressed signal wraps around azimuth frequency as a result of ambiguity (see Fig. 12a). It may degrade the effectiveness of feature extraction algorithm starting with spectrum. To validate this assumption, a FFT-based time-frequency approach [8] and a complex spectral estimation algorithm called APES [16] are used to extract the spectral envelope of T3 respectively. As shown in Fig. 12b, the extracted results differ from the real data due to the impact of ambiguity. Thus, the proposed M-RANSAC-based feature extraction algorithm, which establishes itself as an ambiguity-free approach, is required in this case. The M-RANSAC-based algorithm starts with time-domain range compressed signal (see Fig. 12c). Its initial parameters are carefully designed. The scale factor ϑ in (10) is set to be 450. The lower bound of iterative times min is 30 and the upper bound max is 200, the threshold of quadratic orthogonal distance rho_thr is 0.003, and the threshold number of inliers N_thr is $0.85N_a$. After estimating $\vec{\mu}$ for the M dominant scattering centers and classifying inliers in *set*, the geographical locations and velocity information are reconstructed based on (23). As shown in the columns $\hat{\boldsymbol{R}}_{\boldsymbol{0}}$, $\hat{\boldsymbol{\eta}}_{\boldsymbol{0}}$, and $\hat{\boldsymbol{V}}_{\boldsymbol{r}}$ of Table 2, the estimated errors are quite limited. Meanwhile, the backscattering envelopes are extracted and normalized. In Fig.11a, the extracted backscattering amplitude envelopes of dominant scattering centers match the theoretical ones of the corresponding targets.

Without knowing the explicit knowledge of platform velocity and forming a SAR image, the extracted backscattering envelopes can label T1 and T2 as azimuth invariant targets and T3 as an azimuth variant target. Thus, a rough target classification can be achieved. $\hat{\boldsymbol{R}}_{\boldsymbol{0}}$ and $\hat{\boldsymbol{\eta}}_{\boldsymbol{0}}$ present the geographical locations of dominant scattering centers. To visualize the extracted information, we map $\hat{\boldsymbol{R}}_{\boldsymbol{0}}$ and $\hat{\boldsymbol{\eta}}_{\boldsymbol{0}}$ of scattering centers into image domain. The amplitudes of them are obtained by averaging their backscattering envelopes. As shown in Fig. 12d, the image is free from the impact of sidelobes. Realizing the target classification and location, M-RANSAC-based algorithm help us to comprehend the targets without forming a SAR image.

When the explicit platform velocity is given, SAR image (see Fig. 12f) can be formed by chirp-scaling algorithm [30, 31]. Figure 12e presents the imaging result with eight times interpolation. In this image, T1 is well-focused while T2 and T3 are defocused. From the perspective of SAR image, T2 and T3 may be mistakenly classified

Table 2 Original and estimated parameters in both simulation test and real data test

Type	Scattering center	$\boldsymbol{R}_{\boldsymbol{0}}$ [m]	$\boldsymbol{\eta}_{\boldsymbol{0}}$ [s]	$\boldsymbol{V}_{\boldsymbol{r}}$[m/s]	$\hat{\boldsymbol{R}}_{\boldsymbol{0}}$[m]	$\hat{\boldsymbol{\eta}}_{\boldsymbol{0}}$[s]	$\hat{\boldsymbol{V}}_{\boldsymbol{r}}$ [m/s]
Simulation	T1	7500	0.8717	153.3	7500.7	0.8703	153.56
	T2	7462.5	0.8717	147.8	7462.2	0.8721	146.62
	T3	7537.5	0.8717	153.3	7538.7	0.8719	153.48
Real data	T1	997743	1.3143	7062.4	997744.3	1.3127	7062.9
	T2	997226	1.4202	7061.8	997226.8	1.4212	7061.9
	T3	997375	1.7073	7061.7	997374.1	1.7097	7061.2
	T4	997582	1.8665	7062.2	997582.5	1.8670	7061.7

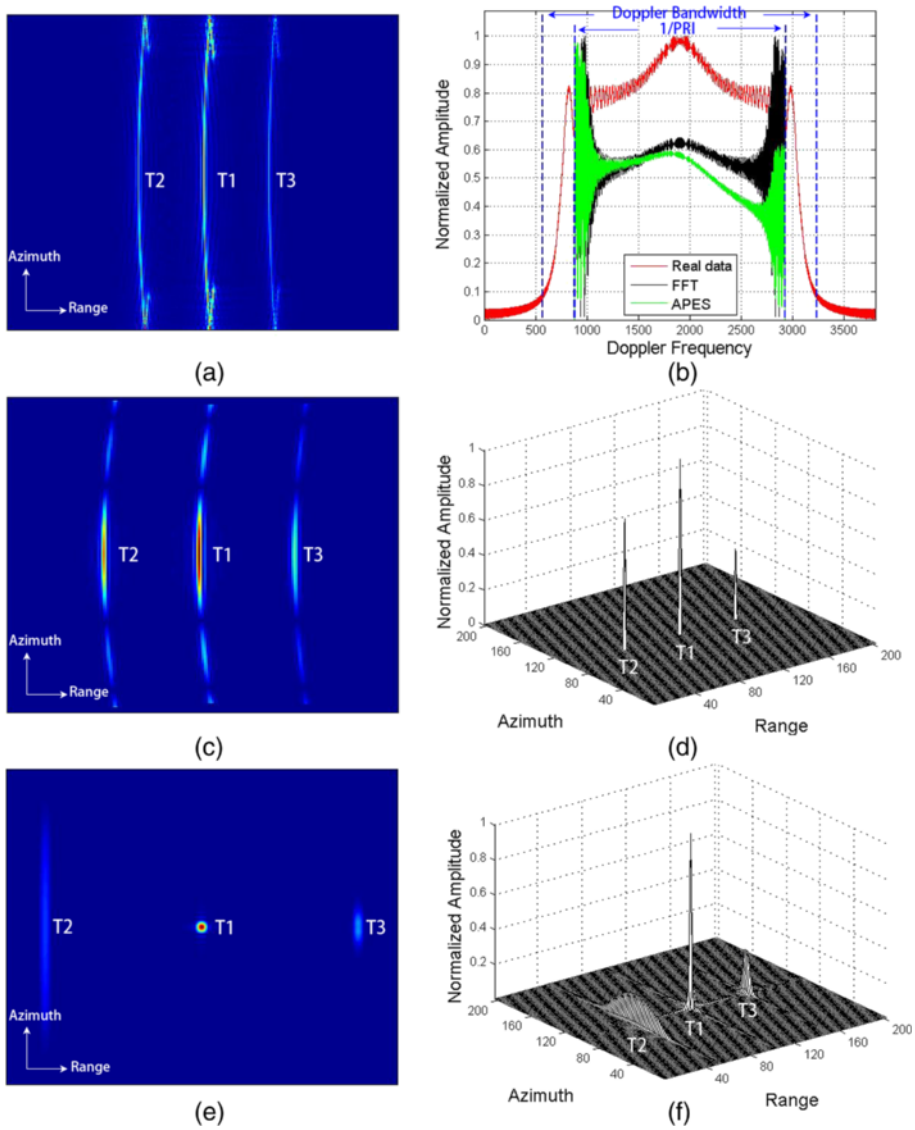

Fig. 12 Simulation test. **a** Doppler spectrum of a range-compressed signal (range-compressed Doppler domain). **b** Extracted spectral envelopes of T3 using FFT and APES. **c** Time-domain range-compressed signal (range-compressed azimuth-time domain). **d** SAR image formed by mapping the extracted feature. **e** SAR image with eight times interpolation formed by chirp-scaling algorithm. **f** SAR image formed by chirp-scaling algorithm

into the same type. However, defocus only indicates the mismatch of azimuth matched filter. It may result from either the along-track motion (T2) or the invariant azimuth envelope (T3). Since the two cases are hardly distinguished directly from SAR image, the importance of feature extraction is proved. The extracted envelopes of dominant scattering centers in Fig. 11a clearly reveals the backscattering feature of targets. Thus, we can label T1 and T2 as azimuth invariant targets and T3 an azimuth variant one. The backscattering envelope of target's dominant scattering center can be complementary to the SAR image in the application of target classification. Moreover, given the explicit platform velocity, we confirm T2 as a moving target according to column $\hat{V}_r$ of Table 2.

6.3 Real data test

In this subsection, RADARSAT-1 raw data included in the CD of [19] is applied in feature extraction. The key system parameters are listed in Table 1. As shown in Fig. 13a, the SAR image of English Bay is formed using the chirp-scaling algorithm. Then, the region of four ships, marked with a white rectangle, are truncated from this SAR image. This patch of complex image is converted to a range-compressed signal (use inverse chirp-scaling algorithm and range matched filter).

As shown in Fig. 13b, the trajectories of RMCs of the ship T2 and T3 are overlapped. Before extracting the feature scatter by scatter, the overlapped trajectories are separated using the STFRFT-based approach. First, K_a is

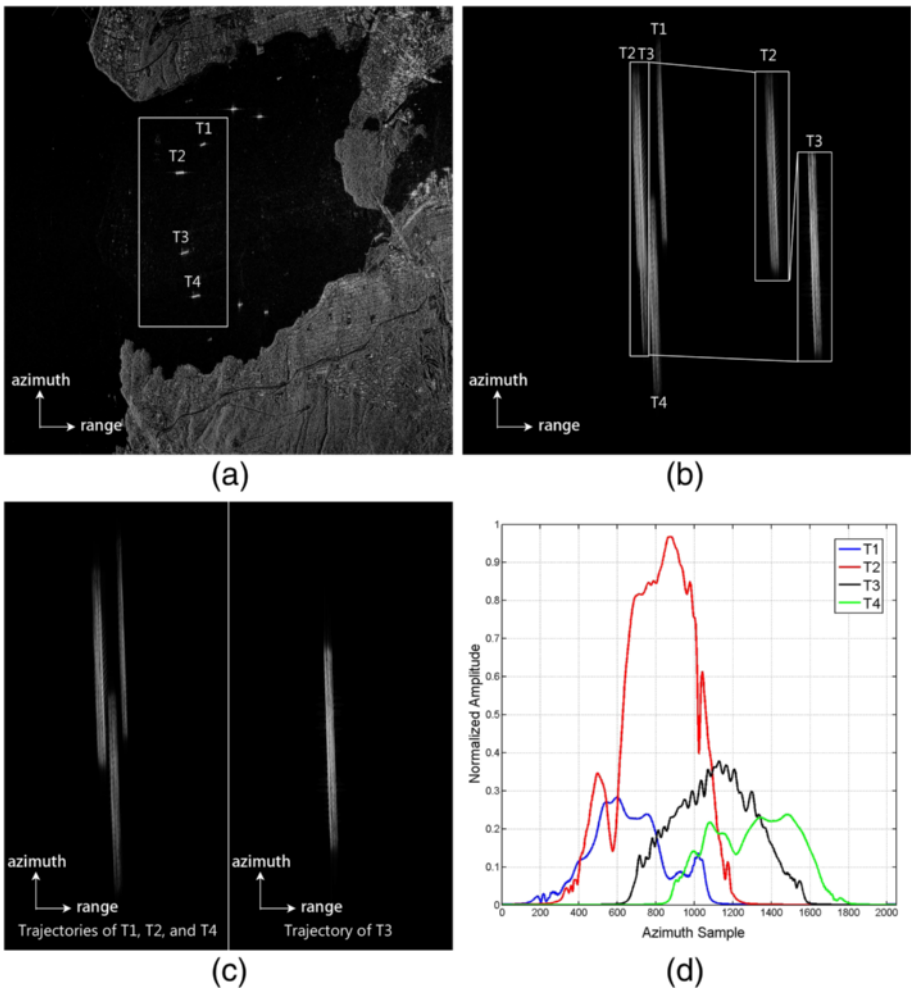

Fig. 13 Experimental results based on RADARSAT-1 data. **a** SAR image formed by chirp-scaling algorithm. **b** Trajectories of RMCs of ships in time-domain range compressed signal. **c** The result of trajectories separation based on STFRFT. **d** Extracted backscattering amplitude envelopes of dominant scattering centers

estimated using the dominant scattering center of isolated ship T1. Then, α is computed by (31). Using α-angle STFRFT and spatial filtering, the energy of T3 are separated from the whole range-compressed signal. After inverse STFRFT, two sub-patch results are obtained (see Fig. 13c).

The M-RASNAC-based feature extraction algorithm starts with the range-compressed signal in Fig. 13c. The scale factor $\vartheta = 5800$ in (10), the lower bound of iterative times min $= 30$, and the upper bound max $= 300$, the threshold of quadratic orthogonal distance rho_thr $=$ 0.0016, and the threshold number of inliers $N\_thr = 0.85 \cdot N_a$. After estimating $\vec{\mu}$ for the dominant scattering centers of each ship, the geographical locations and velocity information are reconstructed based on (22) (see columns $\hat{\boldsymbol{R}}_{\mathbf{0}}$, $\hat{\boldsymbol{\eta}}_{\mathbf{0}}$, and $\hat{\boldsymbol{V}}_{\boldsymbol{r}}$ of Table 2). To verify the performance of parameters construction, we define the dominant scattering center of a ship as the point with maximum amplitude in SAR image. Their geographical locations are listed in columns $\boldsymbol{R}_{\mathbf{0}}$ and $\boldsymbol{\eta}_{\mathbf{0}}$ of Table 2. The micro along-track velocity of dominant scattering centers are estimated using fractional Fourier transform (FRFT)-based method introduced in [32]. The relative velocity between radar platform and these scattering centers are then listed in column $\hat{\boldsymbol{V}}_{\boldsymbol{r}}$ of Table 2. Since two groups of data are in good agreements, the reconstructed errors are quite limited.

Then, to better understand the targets, the backscattering envelopes of dominant scattering centers are extracted from the range-compressed signal. As shown in Fig. 13d, T1 is much brighter than the others which may indicate the a relatively higher radar cross section (RCS) [29]. Moreover, T2 and T3 are azimuth variant while T1 and T4 are nearly azimuth invariant. It means the illuminated regions of T2 and T3 are more "flat" than those of T1 and T4.

7 Conclusions

An M-RANSAC and STFRFT-based technique is introduced to extract feature of SAR dominant scattering centers in this paper. Starting with the time-domain range-compressed signal, this algorithm provides an ambiguity-free signal-level approach. Meanwhile, this algorithm requires no explicit knowledge of platform velocity. It can conduct feature extraction without forming a SAR image. Within the extracted features, the backscattering envelope is promising to classify the target type in signal level, the geographical location indicates the target position relative to SAR platform, and the relative velocity denotes the along-track motion of illuminated target.

Experiments are conducted to illustrate the performance of this algorithm. In the tests, the estimation errors of location and relative velocity are quite limited when SNR is relatively high. The normalized extracted backscattering envelopes express their theoretical ones well. Moreover, these extracted features validate their usage in target recognition and classification. Without forming a SAR image, these extracted features will help us roughly understand and classify the illuminated targets. When SAR image is formed by conventional methods, the extracted backscattering envelopes can be complementary to SAR image in the application of target recognition and classification.

Competing interests

The authors declare that they have no competing interests.

Acknowledgements

This work has been supported by key project of the National Natural Science Foundation (NNSF) of China (nos.61132005). The authors also want to express gratitude to editors and anonymous reviewers who give the helpful comments and suggestions to his paper.

Received: 2 July 2015 Accepted: 31 March 2016
Published online: 12 April 2016

References

1. DE Dudgeon, RT Lacoss, An overview of automatic target recognition. Lincoln Lab J. **6**(1), 3–10 (1993)
2. GJ Owirka, SM Verbout, LM Novak, in *AeroSense'99*. Template-based SAR ATR performance using different image enhancement techniques (SPIE, Bellingham WA 98227-0010 USA, 1999), pp. 302–319. International Society for Optics and Photonics
3. Z Jianxiong, S Zhiguang, C Xiao, F Qiang, Automatic target recognition of SAR images based on global scattering center model. IEEE Trans Geosci Remote Sens. **49**(10), 3713–3729 (2011)
4. Y Chen, E Blasch, H Chen, T Qian, G Chen, in *SPIE Defense and Security Symposium*. Experimental feature-based SAR ATR performance evaluation under different operational conditions (SPIE, Bellingham WA 98227-0010 USA, 2008), pp. 69680–69680. International Society for Optics and Photonics
5. Y Huang, J Pei, J Yang, T Wang, H Yang, B Wang, Kernel generalized neighbor discriminant embedding for SAR automatic target recognition. EURASIP J Adv Signal Process. **2014**(1), 1–6 (2014)
6. JB Keller, Geometrical theory of diffraction. JOSA. **52**(2), 116–130 (1962)
7. LC Potter, RL Moses, Attributed scattering centers for SAR ATR. IEEE Trans Image Process. **6**(1), 79–91 (1997)
8. M Spigai, C Tison, J-C Souyris, Time-frequency analysis in high-resolution SAR imagery. IEEE Trans Geosci Remote Sens. **49**(7), 2699–2711 (2011)
9. VC Chen, H Ling, *Time-Frequency Transforms for Radar Imaging and Signal Analysis*. (Artech House, Norwood, 2001)
10. J-P Ovarlez, L Vignaud, J-C Castelli, M Tria, M Benidir, Analysis of SAR images by multidimensional wavelet transform. IEE Proc Radar Sonar Navig. **150**(4), 234–241 (2003)
11. G Lisini, C Tison, F Tupin, P Gamba, Feature fusion to improve road network extraction in high-resolution SAR images. IEEE Geosci Remote Sens Lett. **3**(2), 217–221 (2006)
12. Z-S Liu, J Li, in *Radar, Sonar and Navigation, IEE Proceedings-*. Feature extraction of SAR targets consisting of trihedral and dihedral corner reflectors, vol. 145 (IET, Michael Faraday House, Six Hills Way Stevenage, Herts, SG1 2AY, UK, 1998), pp. 161–172
13. Z Bi, J Li, Z-S Liu, Super resolution SAR imaging via parametric spectral estimation methods. IEEE Trans Aerosp Electron Syst. **35**(1), 267–281 (1999)
14. J Li, P Stoica, Efficient mixed-spectrum estimation with applications to target feature extraction. IEEE Trans Signal Process. **44**(2), 281–295 (1996)
15. EG Larsson, G Liu, P Stoica, J Li, High-resolution SAR imaging with angular diversity. IEEE Trans Aerosp Electron Syst. **37**(4), 1359–1372 (2001)
16. J Li, P Stoica, An adaptive filtering approach to spectral estimation and SAR imaging. IEEE Trans Signal Process. **44**(6), 1469–1484 (1996)
17. SR DeGraaf, Sidelobe reduction via adaptive FIR filtering in SAR imagery. IEEE Trans. Image Process. **3**(3), 292–301 (1994)
18. R Wu, J Li, Z Bi, P Stoica, SAR image formation via semiparametric spectral estimation. IEEE Trans Aerosp Electron Syst. **35**(4), 1318–1333 (1999)
19. IG Cumming, FH-c Wong, *Digital Processing of Synthetic Aperture Radar Data: Algorithms and Implementation*. (Artech House, Norwood, 2005)
20. R Tao, Y-L Li, Y Wang, Short-time fractional Fourier transform and its applications. IEEE Trans Signal Process. **58**(5), 2568–2580 (2010)
21. SJ Ahn, W Rauh, H-J Warnecke, Least-squares orthogonal distances fitting of circle, sphere, ellipse, hyperbola, and parabola. Pattern Recogn. **34**(12), 2283–2303 (2001)
22. YC Cheng, SC Lee, A new method for quadratic curve detection using K-RANSAC with acceleration techniques. Pattern Recogn. **28**(5), 663–682 (1995)
23. PH Torr, A Zisserman, MLESAC: a new robust estimator with application to estimating image geometry. Comput Vis Image Underst. **78**(1), 138–156 (2000)
24. J Tsao, BD Steinberg, Reduction of sidelobe and speckle artifacts in microwave imaging: the CLEAN technique. IEEE Trans. Antennas Propag. **36**(4), 543–556 (1988)
25. H Deng, Effective CLEAN algorithms for performance-enhanced detection of binary coding radar signals. IEEE Trans Signal Process. **52**(1), 72–78 (2004)
26. HM Ozaktas, O Arikan, MA Kutay, G Bozdagi, Digital computation of the fractional Fourier transform. IEEE Trans. Signal Process. **44**(9), 2141–2150 (1996)
27. S Chiu, Application of fractional fourier transform to moving target indication via along-track interferometry. EURASIP J Appl Signal Process. **2005**, 3293–3303 (2005)
28. TA Schonhoff, AA Giordano, *Detection and Estimation Theory and Its Applications*. (Pearson/Prentice Hall, New Jersey, 2006)
29. EF Knott, *Radar Cross Section Measurements*. (SciTech Publishing, Raleigh, 2006)
30. RK Raney, H Runge, R Bamler, IG Cumming, FH Wong, Precision SAR processing using chirp scaling. IEEE Trans Geosci Remote Sens. **32**(4), 786–799 (1994)
31. A Moreira, J Mittermayer, R Scheiber, Extended chirp scaling algorithm for air- and spaceborne SAR data processing in stripmap and ScanSAR imaging modes. IEEE Trans Geosci Remote Sens. **34**(5), 1123–1136 (1996)
32. J Yang, C Liu, Y Wang, Detection and imaging of ground moving targets with real SAR data. IEEE Trans Geosci Remote Sens. **53**, 920–932 (2015)